ACS APPLIED ELECTRONIC MATERIALS

pubs.acs.org/acsaelm

Article

Optimization and Validation of the Thermochromic Performance of a Trilayer Coating of $TiO_2/VO_2/TiO_2$ for Smart Windows

Martin Becker,* Yan Ravil Wollenweber-Bienerth, Saskia Hartmann, Angelika Polity, Sangam Chatterjee, and Peter J. Klar

Cite This: *ACS Appl. Electron. Mater.* 2025, 7, 7668−7678

Read Online

ACCESS | Metrics & More | Article Recommendations | Supporting Information

ABSTRACT: Global energy consumption and the imperative to mitigate climate change have driven the exploration of innovative technologies to enhance energy efficiency in buildings. Among these, smart windows utilizing thermochromic vanadium dioxide-based materials as active materials have emerged as a promising avenue. These windows dynamically modulate their optical properties in response to environmental conditions, helping to reduce the energy consumption for heating/cooling of the building. However, the practical implementation of VO_2-based smart windows faces challenges related to optimizing their performance and durability. In this context, this review advocates for further research into VO_2-based smart windows incorporating titanium dioxide (TiO_2) buffer layers and TiO_2 antireflection (AR) coatings. Rutile TiO_2 buffer layers are used to promote growth of the VO_2 functional films. Additionally, TiO_2 antireflection coatings can improve the optical performance of smart windows by minimizing reflections and maximizing light transmission. This work highlights how TiO_2-based layers may be used to form a multilayer system surrounding the active VO_2 layer in order to enhance the efficiency of VO_2-based smart windows. The proposed application of rutile TiO_2 buffer layers and anatase TiO_2 AR layers holds promise for advancing the development of energy-efficient building technologies.

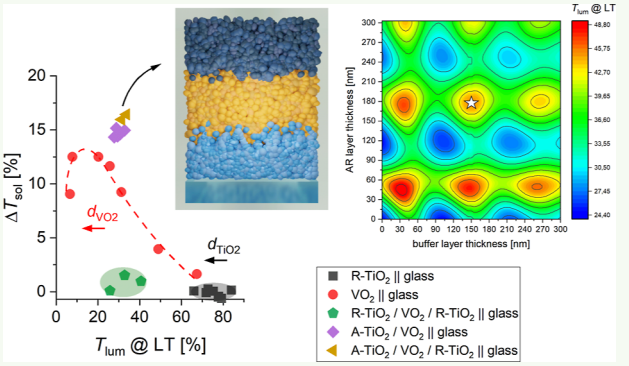

KEYWORDS: *ion-beam sputter deposition, smart windows, thermochromism, vanadium dioxide, titanium oxide*

INTRODUCTION

The escalating global energy consumption and the urgent necessity for cooling due to the effects of global warming have thrust the world into the throes of severe ecological challenges. Addressing these challenges demands innovative solutions, and smart window glazing technology emerges as a promising avenue to partially alleviate future energy demands.[1−4] These advancements in glazing technology are engineered to dynamically regulate the transmission of light across both the visible and infrared spectra, responding to fluctuations in external temperature conditions.

Vanadium dioxide (VO_2) stands out prominently among the thermochromic materials studied thus far. Its notable feature lies in its abrupt switching of infrared (IR) transparency at a critical phase transition temperature (θ_c) of 68 °C. This transition, from a high transmission of IR light to substantial IR reflectance, is concomitant with a semiconductor-to-metal transition and a structural phase transition from a monoclinic (M1) to a rutile (R) crystal structure.[5] Ke et al. have summarized the application of suitable external stimuli (i.e., photons, heat, electric, magnetic, electrochemical, and stress) to initiate the transition in VO_2-based devices.[6] Notably, VO_2 exhibits different low-temperature phases (M1, T, and M2), which can be stabilized by doping, strain, or stoichiometry engineering.[7−9] Despite these advantages, binary VO_2 presents limitations for practical applications, primarily due to its high phase transition temperature and low band gaps, resulting in undesirable brownish hues in glazing.

Doping emerges as the most prevalent strategy to enhance the properties of VO_2. In this approach, metal atoms substitute for vanadium atoms in the host lattice, yielding Me-doped $V_{1-x}Me_xO_2$ thin films. Among these dopants, tungsten has been identified as particularly effective.[10−13] Various methods can be employed to modify the color impression of VO_2 layers, including thickness variation, the integration of VO_2 nanoparticles within a transparent matrix, or atomic-level doping.[14−16] Particularly noteworthy is the doping of VO_2 with alkaline earth metals on vanadium sites, significantly

Received: May 21, 2025
Revised: July 8, 2025
Accepted: July 9, 2025
Published: August 6, 2025

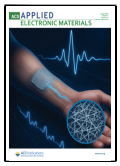

widening the band gap and resulting in a neutral grayish color impression in thin films.[17]

Key parameters for evaluating the optical properties of thermochromic layers include luminous transmittance (T_{lum}) and solar transmittance (T_{sol}). T_{lum} characterizes integral transmission in the visible spectrum, weighted by the spectral sensitivity of the human eye, while T_{sol} describes integral transmission across the entire AM 1.5 solar spectrum. Recent research has unveiled the potential of codoping VO_2 with strontium (Sr) and tungsten (W), yielding quaternary $V_{1-x-y}Sr_xW_yO_2$ thin films that meet nearly all requirements.[11,18,19]

Further advancements are anticipated through the integration of the thermochromic layer into a multilayer system.[18,20−23] For instance, multilayer systems composed of alternating thin layers of VO_2 and TiO_2 exhibit an antireflection effect, leading to a higher transmittance. Hybrid layers comprising VO_2 nanoparticles embedded in dielectric matrices have demonstrated the capability to increase luminous transmittance (T_{lum}) by adjusting the effective optical properties, such as the refractive index. Suzuki et al. employed a sol−gel technique to deposit VO_2 layers onto SiO_2 nanoparticles, resulting in a hybrid material with significantly elevated T_{lum}, thereby reversing the aforementioned structure.[14] Through this investigation, it was revealed that the crystal structure and morphology of undoped VO_2 exert a significant influence on its optical properties. Some researchers have noted that increasing the porosity of VO_2 thin films alters their dielectric properties, thereby enhancing T_{lum}.[24−26] An alternative approach involves avoiding direct growth on the substrate surface and instead establishing a well-defined buffer layer in between.[23,27,28] To manage interfacial strain and stress in an epitaxial film, the lattice parameters must be taken into account. As a guiding principle, selecting a substrate with structural similarity, low lattice mismatch, and similar chemistry is the optimal strategy for promoting a specific polytype of the deposited material. In context of VO_2-based smart windows, titanium dioxide (TiO_2) buffer layers have garnered significant attention due to the matching crystal structure between rutile TiO_2 and the high-temperature phase of VO_2. Zhang et al. conducted pioneering investigations on VO_2 films deposited on TiO_2 substrates using transmission electron microscopy (TEM).[29] Muraoka et al. observed that compressive strain along the *c*-axis of very thin VO_2 films on rutile TiO_2 (100) and (110) substrates leads to a reduction of the transition temperature (θ_c).[30] Fan et al. confirmed that the θ_c in the interface region of epitaxial VO_2 films on rutile TiO_2(001) grown by oxide molecular beam epitaxy can be adjusted by the strain state.[31] Similar results were obtained on rutile TiO_2(110); the buffer-induced strain gradient along the growth direction of the VO_2 film leads to a sequential switching of layer-like regions of the film into the metallic state.[32] Becker et al. performed a systematic evaluation of the impact of TiO_2 buffer layers of different phases and thicknesses on the optical properties of VO_2.[33] They deposited TiO_2 thin films of amorphous, anatase, and rutile phase on sapphire substrates by ion-beam sputter deposition (IBSD) and used them as buffer layers for VO_2. They found that diffusion effects significantly affect the optical performance of the VO_2 film on the top. Furthermore, the influence of amorphous and crystalline TiO_2 on the VO_2 properties considerably differs, and only rutile TiO_2 buffer layers provide the possibility to lower the growth temperature onset for the functional VO_2 thin film. There have also been other reports advocating the use of TiO_2 in the anatase phase in combination with VO_2.[34,35] However, regardless of the polytype of TiO_2, careful adjustment of both the buffer layer thickness and VO_2 layer thickness is imperative. Increasing the thickness of the VO_2 layer allows for gradual relaxation of the VO_2 film, eventually exhibiting semiconductor-to-metal transition (SMT) behavior akin to that of the bulk material. Additionally, VO_2 films have been observed to maintain an intermediate strain state over a broader range of film thicknesses on buffer layers, whereas VO_2 films on single-crystalline TiO_2 substrates relax almost instantaneously. Furthermore, the TiO_2 buffer serves as a barrier layer for ion diffusion from glass substrates.[36]

Opting for a multilayer approach, however, offers additional opportunities, as well as challenges. Controlling the surface morphology of thin films is of paramount importance across a broad spectrum of technological applications, as it directly impacts physical, chemical, and electronic properties. In semiconductor device fabrication, for example, the atomic-scale arrangement at the surface critically influences charge carrier mobility and overall device performance, thereby underpinning the development of faster and more efficient electronic components.[37] Similarly, in photovoltaic systems, the surface structure of thin films plays a vital role in modulating light absorption and enhancing energy conversion efficiency.[38] In catalytic processes, the morphology of thin films determines the nature and distribution of active sites, thereby affecting catalytic activity and selectivity.[39] Consequently, precise control over surface morphology is mandatory for optimizing the functional performance in various fields. In the context of VO_2-based multilayer architectures for smart windows, the morphology of the interfaces between the active VO_2 layer and adjacent layers can affect the optical as well as the thermochromic properties of a multilayer stack. The optical properties of the stack are determined not only by the materials comprising the stack but also by the refractive index profile along the stack and the chosen layer thicknesses. In this context, microscopic diffusion across the interface or interface roughness will affect the refractive index profile as well as cause an effective deviation from the ideal layer thicknesses. Furthermore, an interface with roughness on the micrometer scale may also lead to diffuse scattering of light, which also alters the transmittance through the entire stack. The thermochromic properties, in particular, the transition temperature, may be affected by unintentional doping caused by interdiffusion across the interface or strain induced by the interface as discussed above. Hence, the impact of the interface morphology on the thermochromic and optical properties of a thermochromic multilayer stack cannot be universally predicted, as the interface morphology may vary in various ways. Our modeling approach of the interface roughness is rather simple and based on effective medium theory only, as discussed in detail below.

In this study, our focus centers on a trilayer system comprising a TiO_2 buffer layer, a thermochromic VO_2 layer, and an additional TiO_2 layer serving as an antireflection coating in the visible spectrum. Our investigation will delve into the influence of surrounding layers on key parameters (T_{lum}, T_{sol}, ΔT_{lum}, and ΔT_{sol}) and compare experimental results with corresponding simulations using the Essential Macleod software package.

https://doi.org/10.1021/acsaelm.5c01043
ACS Appl. Electron. Mater. 2025, 7, 7668−7678

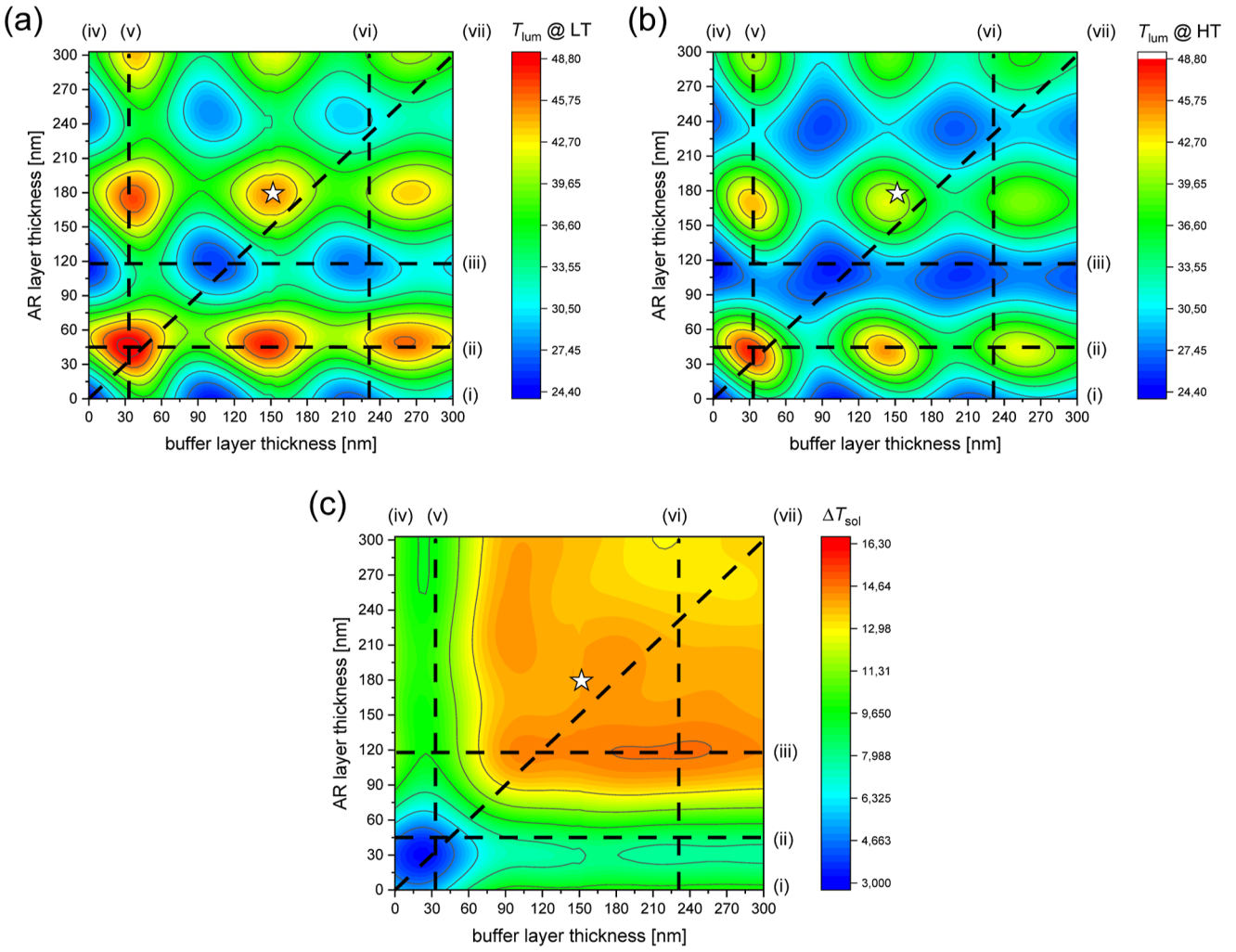

Figure 1. Contour maps of the TC key quantities of an A-TiO_2/VO_2/R-TiO_2 stack on the quartz glass substrate. (a) T_{lum} (25 °C), (b) T_{lum} (90 °C), and (c) ΔT_{sol} as a function of thickness of the R-TiO_2 buffer layer (*x*-axis) and that of the A-TiO_2 AR layer (*y*-axis) with a fixed thickness of VO_2 of 50 nm. The optical constants determined by ellipsometry were used for the calculation. The dashed vertical lines mark thicknesses of 0, 33, and 231 nm, respectively. Those thicknesses correspond to single buffer or AR layers (0 nm), the first order maximum and, thus, global maximum of T_{lum} (33 nm) and the global maximum of ΔT_{sol} (231 nm). The dashed horizontal lines mark thicknesses of 0, 45, and 118 nm, respectively. Those thicknesses correspond to single buffer or AR layers (0 nm), the first order maximum and, thus, global maximum of T_{lum} (45 nm) and the global maximum of ΔT_{sol} (118 nm). The thickness combination of buffer and AR layer that give the best combination of ΔT_{sol} and T_{lum} values is marked with an asterisk.

EXPERIMENTAL PROCEDURES

We deposit TiO_2 (rutile R-TiO_2 and anatase A-TiO_2) and VO_2 films using a customized ceramic TiO_2 target and a metallic V target (99.9% purity, Beijing Goodwill Metal Technology Co.), respectively. We employ ion-beam sputter deposition for TiO_2 as well as VO_2.[33,40] Further information on the distinct sputter setup and ion-beam sputter deposition (IBSD) in general can be found elsewhere.[41] A quartz glass is used as the substrate.

Raman spectroscopy is employed to identify the phases of TiO_2 and VO_2 thin films. The morphology of the films is examined by using scanning electron microscopy (SEM) with an InLens detector on a Merlin (ZEISS) system. Atomic force microscopy (AFM) measurements are performed with a Bruker Dimension Icon instrument (Multimode 8), utilizing ScanAsyst Air AFM probes in ScanAsyst mode to assess the surface roughness of the films. The AFM data are analyzed using the Gwyddion software package. The optical constants, specifically the refractive index (*n*) and extinction coefficient (*k*), of TiO_2 and VO_2 are measured at temperatures of 25 and 90 °C using an ellipsometer (SENresearch 4.0, Sentech) featuring a custom-designed heating stage. The dispersions of the optical constants (*n*, *k*) of the layer materials employed are then used for simulating the optical response of the TiO_2/VO_2/TiO_2 layer stack on a quartz glass substrate. Essential MacLeod software is used for the simulations. Based on the simulation results, which map the parameter space of buffer layer and AR layer thicknesses, the optimal thickness of the TiO_2 layers in a TiO_2/VO_2/TiO_2||glass structure is determined. The layer thicknesses are considered optimal when the combination of values of the key quantities of the thermochromic smart window is best, i.e., the luminous transmittance (T_{lum}) and the solar modulation ability (ΔT_{sol}) both exhibit high values.

Based on the simulated thermochromic properties, we prepared TiO_2||glass, VO_2/TiO_2||glass, and TiO_2/VO_2/TiO_2||glass samples with optimized thicknesses to validate the impact of buffer and antireflective (AR) layers on the thermochromic properties of the multilayer structure. Spectral transmittance measurements across the range of 300−3000 nm were conducted at both 25 and 90 °C using a UV−Vis−NIR spectrometer (Lambda 900, PerkinElmer) with a custom heating setup. The thermochromic parameters, T_{lum} and T_{sol}, are derived from the optical transmittance $T(\lambda)$.[33] Given that these parameters vary with the specific VO_2 polytype, we also assess the relative changes in T_{lum} and T_{sol} due to phase transitions, referred to

https://doi.org/10.1021/acsaelm.5c01043
ACS Appl. Electron. Mater. 2025, 7, 7668−7678

as ΔT_{lum} and ΔT_{sol}. Here, especially the solar modulation ability ΔT_{sol} is crucial for enhancing the device performance.

RESULTS AND DISCUSSION

We conducted both experiments and simulations to better understand the impact and interplay of the three layers of the thermochromic multilayer coating, $TiO_2/VO_2/TiO_2$ on a quartz glass substrate, on its thermochromic properties. For this purpose, we deposited VO_2 films on quartz glass with an R-TiO_2 buffer layer (TiO_2-1) and an R-TiO_2 antireflective layer (TiO_2-2a). R-TiO_2, VO_2, and VO_2/R-TiO_2 films were deposited on the quartz glass substrate at 550 °C.

We performed X-ray diffraction and Raman spectroscopy to verify the material's phases, cf. Figure S1 in the Supporting Information. Especially Raman spectroscopy proved suitable to detect minor crystalline inclusions; for comparison with literature, see refs 42−44. The optical constants of R-TiO_2 and VO_2 were measured using ellipsometry at 25 and 90 °C as a function of wavelength. For this purpose, layers of R-TiO_2 and VO_2 were grown on Si wafers with 275 nm of thermal oxide. No noticeable change in the optical constants of the R-TiO_2 film was observed when varying the temperature between 25 and 90 °C. In contrast, the optical constants switch at the insulator to metal transition in the VO_2 films and thus differ for 25 and 90 °C (for corresponding ellipsometry measurements, see Figure S2 in the Supporting Information). A layer sequence of X||SiO_2||Si with X = R-TiO_2, VO_2 was used in the fitting procedure employed for extracting the optical parameters from the ellipsometry data. Here, the dispersion relations of Verleur et al. and Voloshenko et al. were used as starting points for fitting the data of low-temperature (LT) monoclinic VO_2 and high-temperature (HT) rutile HT-VO_2, respectively.[45−47] The optical constants of the R-TiO_2 and VO_2 films obtained were then used for the simulation of the thermochromic key quantities. Here, the measured optical constants of the R-TiO_2 buffer layer were used for the AR layer as well since the deposition conditions of the two layers were the same. With that, a systematic variation of the thicknesses of the buffer and AR layers in the simulations of multilayer structures allows us to identify optimized thermochromic properties. In the first step, we calculate the thermochromic key quantities as a function of the thickness of the buffer and AR layers, d_{buffer} and d_{AR}, each varying from 0 to 300 nm. The VO_2 layer thickness was kept constant at 50 nm. The simulation results are shown in Figure S3 in the Supporting Information for (b) $T_{lum}(d_{buffer}, d_{AR})$ at 25 °C, (c) $T_{lum}(d_{buffer}, d_{AR})$ at 90 °C, and (d) $\Delta T_{sol}(d_{buffer}, d_{AR})$.

Unfortunately, adding an R-TiO_2 layer as an AR coating experimentally caused the multilayer structure to lose its thermochromic performance. We suspect that the growth conditions are responsible for this observation, as it is known that deposition of rutile TiO_2 via ion-beam sputtering techniques requires elevated temperatures at high oxygen flux.[33] These conditions may trigger the surface of the subjacent functional VO_2 layer to convert into a phase of the higher vanadium oxidation state. To verify these assumptions, we simulated the thermochromic key quantities T_{lum} (25 °C) and ΔT_{sol} as a function of thickness of the buffer layer (x-axis) and that of the AR layer (y-axis) with a fixed thickness of VO_2 of 50 nm. This time, however, we replaced a certain fraction of our VO_2 functional film by V_2O_5. Results of such simulations are shown in Figure S4 in the Supporting Information. Indeed, we observe the thermochromic performance to significantly decrease with reduced VO_2 thickness. Hence, simulations agree well with our experimental findings. As a result, in a first attempt, we have to either reduce the oxygen flux or reduce the growth temperature to avoid formation of V_2O_5. Following both options, however, we will fail to create rutile TiO_2. To solve this, we decided to indeed lower the growth temperature and to work with anatase TiO_2 as an antireflection/capping layer instead of rutile TiO_2.

To optimize the thermochromic properties of our VO_2 films deposited on quartz glass with a R-TiO_2 buffer layer (TiO_2-1) and an A-TiO_2 AR layer (TiO_2-2b), again both experiments and simulations were carried out. The optical constants of A-TiO_2 were determined using ellipsometry at temperatures of 25 and 90 °C across a range of wavelengths. Based on these measurements, we computed the key thermochromic parameters as functions of the thicknesses of the buffer and antireflective (AR) layers, denoted as d_{buffer} and d_{AR}, varying from 0 to 300 nm. The thickness of the VO_2 layer was consistently maintained at 50 nm. The simulation results are presented in Figure 1: (a) $T_{lum}(d_{buffer}, d_{AR})$ at 25 °C, (b) $T_{lum}(d_{buffer}, d_{AR})$ at 90 °C, and (c) $\Delta T_{sol}(d_{buffer}, d_{AR})$.

First, we discuss how T_{lum} is influenced by the thickness of the buffer layer and the AR layer. Their interplay leads to interference effects, evident in the peaks and troughs that occur as we vary the thickness of the two layers. This phenomenon is consistent at the two temperatures studied, as illustrated in Figure 1a,b. For these analyses, we maintained a constant VO_2 thickness of 50 nm. A deeper investigation reveals why the literature often favors the first-order interference maximum when determining the ideal thickness for the buffer and/or AR layers. Specifically, opting for the first-order maximum of T_{lum} offers two significant benefits: it typically yields a higher maximum value, and its broader peak results in a more forgiving deposition process in terms of time and rate. However, utilizing these specific thicknesses for the buffer and AR layers comes with a notable trade-off, as it substantially reduces the solar modulation capability, indicated by $\Delta T_{sol}(d_{buffer}, d_{AR})$ shown in Figure 1c. In other words, the first-order maximum of T_{lum} aligns closely with the overall minimum of $\Delta T_{sol}(d_{buffer}, d_{AR})$. In contrast, when we consider the second-order interference maximum with respect to the thickness of the buffer and AR layers, we find that the T_{lum} maximum coincides with a region exhibiting a higher ΔT_{sol}. Therefore, leveraging the second-order maximum allows for significantly improved solar modulation (ΔT_{sol}) with only a modest reduction in T_{lum}. As a result, we choose to utilize the second-order interference maximum (denoted by an asterisk in the graphs of Figure 1) as it provides a much greater ΔT_{sol} while only slightly lowering T_{lum}. Similar trends have been observed in $ZrO_2/V_{1-x}W_xO_2/ZrO_2$[48] and AlN/$VO_2$/AlN coatings.[22] In our scenario, we anticipate an overall increase of up to 20% in T_{lum} and up to 10% in ΔT_{sol} by selecting the optimal combination of buffer and AR layer thicknesses.

In the following, we analyze the correlation between ΔT_{sol} and T_{lum} further. For this purpose, we plot ΔT_{sol} against T_{lum} measured at 25 °C, as shown in Figure 2. We then analyze $\Delta T_{sol}(T_{lum})$ based on the simulation results along the dashed lines indicated in Figure 1. The subfigures (a−f) in Figure 2, each corresponding to the data along a specific dashed line in Figure 1a, are also annotated with the labels (i) to (vii) to indicate the correspondence. All curves exhibit the same S-shaped behavior. The shapes of the curves vary based on the thickness of the buffer layer (a−c), of the AR layer (d−f), or of

https://doi.org/10.1021/acsaelm.5c01043
ACS Appl. Electron. Mater. 2025, 7, 7668−7678

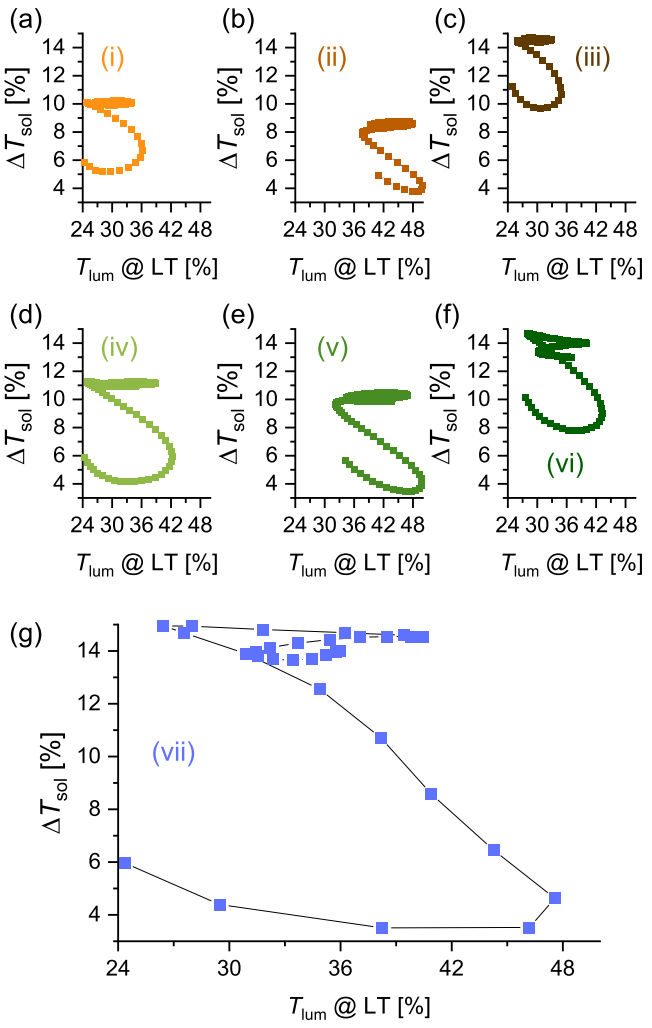

Figure 2. ΔT_{sol} as a function of T_{lum} at 25 °C. Subfigures (a–g) illustrate the curves parametrized along the dashed lines (i–vii) included in Figure 1 and, thus, correspond to an increase in buffer layer thickness (a–c), AR layer thickness (d–f), or similar buffer/AR thickness (g).

both layers when the buffer and AR layer are of equal thickness (g). In subfigure (g), arrows illustrate the trend in $\Delta T_{sol}(T_{lum})$ as thickness increases. Additionally, it is important to note that the upper section of the S-shaped curves more distinctly showcase an oscillating pattern between higher and lower T_{lum} values. The other curves in subfigures (a) to (f) demonstrate a comparable behavior but differ in terms of their position within the $T_{lum}-\Delta T_{sol}$ space. This allows us to discuss the curve progression in more general terms.

All curves start at low T_{lum} and ΔT_{sol} values, with ΔT_{sol} potentially being negative, particularly for smaller VO_2 thicknesses. As the buffer/AR layer thickness increases, the T_{lum} initially rises. However, further increases in thickness lead to a decrease in T_{lum} while ΔT_{sol} increases. This pattern is followed by a secondary increase in T_{lum}, during which ΔT_{sol} remains comparatively stable. As the thickness continues to increase, T_{lum} oscillates between higher and lower values, while ΔT_{sol} gradually declines. Therefore, in pursuit of maximizing both T_{lum} and ΔT_{sol}, we will concentrate on thicknesses located in the upper right quadrant of the S-shaped curve. Specifically, the data point (T_{lum}, ΔT_{sol}) presenting the best option for an experimental realization should be near the first reversal point on the theoretical S-curve, where both T_{lum} and ΔT_{sol} reach their peak values. Notably, in Figure 2g, this optimal point corresponds to a symmetric buffer/AR design with approximately 150 nm of TiO_2. However, since the buffer layer and AR layer are made of different polytypes of the same material, the optimal pair of thicknesses of the two layers that yields the best combination of ΔT_{sol} and T_{lum} (denoted by the asterix symbol in Figure 1) is not located on the dashed line (vii). This is a key distinction when comparing the results shown in Figure 1 with those in Figure S3 of the Supporting Information where simulation results for the case where buffer and AR layer are of the same materiel, i.e., R-TiO_2.

Thus, in the case of the ideal A-TiO_2/VO_2/R-TiO_2||glass structure, the theoretical enhancements of ΔT_{sol} and T_{lum} are 8% and 25%, respectively, compared to the values for a bare VO_2 layer on quartz glass substrate. These values are anticipated for an R-TiO_2 buffer layer of 152 nm and an A-TiO_2 AR layer of 178 nm. This result is based on the assumptions that the layers in the multilayer stack are (I)

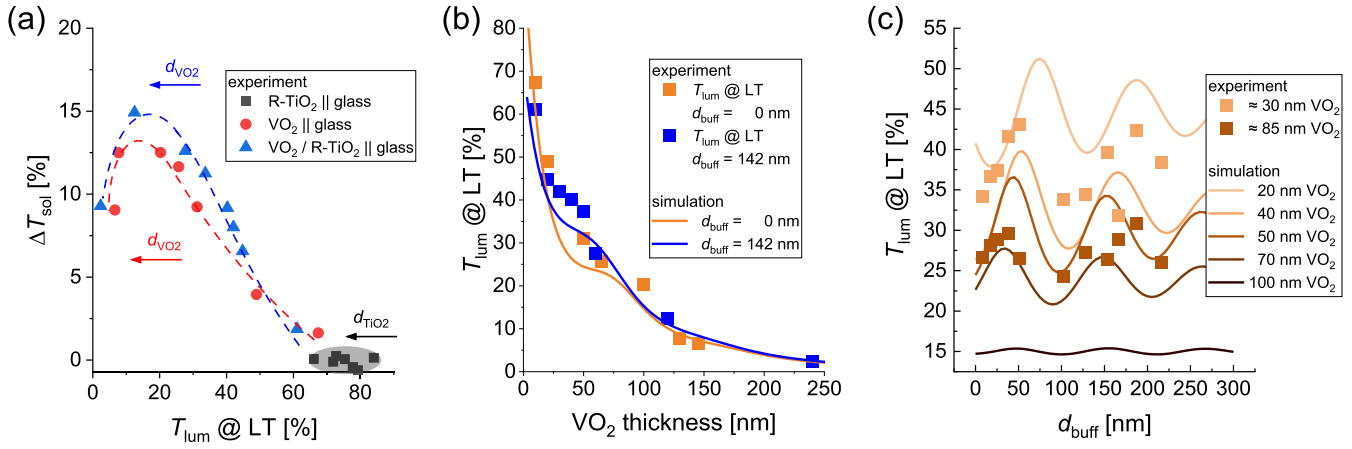

Figure 3. (a) Combined plot of ΔT_{sol} and T_{lum} at 25 °C for architectures R-TiO_2||glass, VO_2||glass, and VO_2/R-TiO_2||glass with different thicknesses of buffer-TiO_2 and of functional VO_2. Arrows emphasize how in each series of samples, the increased layer thickness affects T_{lum}. (b) T_{lum} as a function of the thickness of the VO_2 film on glass as well as on R-TiO_2 of 142 nm thickness. Dependence of T_{lum} on the buffer thickness (c). In (c), VO_2 of different thicknesses is denoted by the different colorations. In all subfigures, symbols denote experimental results, whereas lines represent simulated data.

https://doi.org/10.1021/acsaelm.5c01043
ACS Appl. Electron. Mater. 2025, 7, 7668–7678

perfectly even (with zero roughness on the film surface/interface) and (II) uniform concerning their optical constants (with no porosity) regardless of the individual layer's thickness. Although these assumptions may not reflect reality, the simulations presented provide a framework for optimizing multilayer architecture.

Now we will focus on the thermochromic properties of the different structures grown by IBSD. We begin by comparing the structures R-TiO_2||glass, VO_2||glass, and VO_2/R-TiO_2||glass with varying target thicknesses of the R-TiO_2 buffer and functional VO_2 layers. Figure 3a presents a combined plot showcasing the key quantities ΔT_{sol} and T_{lum} measured at 25 °C. The black squares represent the measurements obtained from the R-TiO_2||glass structures, which serve as reference points. It is evident that increasing the thickness of a single R-TiO_2 layer reduces the luminous transmittance, yet it does not exhibit thermochromic properties, resulting in a negligible ΔT_{sol} value that resembles an overall error in transmittance measurements. In contrast, the scenario changes significantly when we examine a single VO_2 layer on a glass substrate, as indicated by the red circles in Figure 3a. Here, the thermochromic properties of VO_2 cause ΔT_{sol} to increase with a greater thickness, although this occurs at the cost of a reduction in T_{lum}. Moreover, for even thicker layers, both ΔT_{sol} and T_{lum} decrease. This phenomenon has been previously addressed by some of the authors in an earlier study.[33] Additionally, Figure 3a includes data for the VO_2/R-TiO_2||glass architectures, where the thickness of VO_2 varies on top of an R-TiO_2 buffer of a fixed thickness. The overall trend reveals that as the VO_2 thickness increases, ΔT_{sol} rises while T_{lum} declines, similar to the pure VO_2 layer. However, the presence of the R-TiO_2 layer offers an extra degree of modulation for both key quantities. This characteristic is also illustrated in the contour plots in Figure 1. Therefore, utilizing buffer and AR layers of various thicknesses allows for an optimization of the key quantities. This optimization is depicted in Figure 3b, which shows T_{lum} as a function of VO_2 thickness for architectures VO_2||glass and VO_2/R-TiO_2||glass. Notably, a steep decline in T_{lum} is observed solely on the basis of VO_2 thickness, a trend evident in both calculated (solid lines) and experimental data (squares). Furthermore, the presence of a plateau, along with its shift corresponding to the buffer thickness, aligns well with the simulation results, as indicated by the lines in Figure 3b.

Figure 3c shows the T_{lum} of VO_2/R-TiO_2||glass architectures from both simulations (solid lines) and experimental data (squares). Here, the experimental data points clearly resemble the simulated curves with maxima and minima. Hence, T_{lum} can be modulated by choosing a suitable buffer layer thickness. Overall, experiments and simulations show a very promising agreement concerning the tendencies of ΔT_{sol} and T_{lum} and, thus, simulations may serve as a helpful tool prior to time-consuming optimization processes.

Figure 4 presents a combined plot of ΔT_{sol} and T_{lum} at 25 °C for various multilayer architectures on a glass. We assess architectures that incorporate a buffer layer and/or an AR layer against the benchmark values of pure R-TiO_2 and pure VO_2, which were previously addressed in Figure 3a. The comparison is limited to structures with a fixed VO_2 thickness of 50 nm. It turns out that the inclusion of an additional anatase AR layer of suitable thickness, cf. simulations in Figure 1, on top of the functional VO_2 thin film can notably improve both key parameters, as indicated by the data points for these

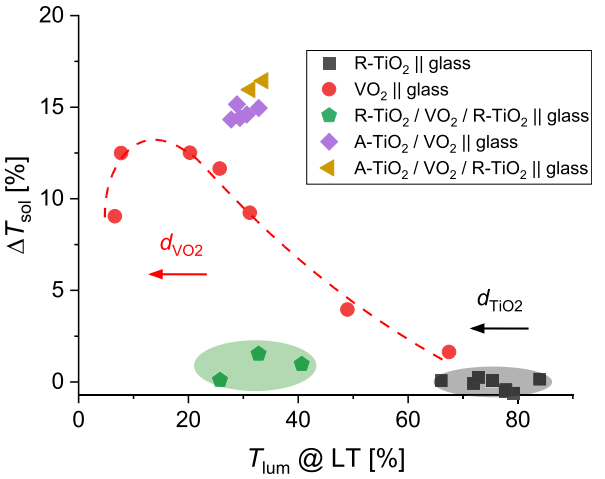

Figure 4. Combined plot of ΔT_{sol} and T_{lum} at 25 °C for different architectures highlighting the benefit of using a multilayer approach with R-TiO2 buffer and A-TiO_2 AR layer. The dashed line is guide to the eye, whereas arrows emphasize how the increased layer thickness for single layers affects T_{lum}.

architectures (diamonds and triangles) being positioned above and to the right of the corresponding single VO_2 thin film data point (circles). Additionally, utilizing both an AR layer and a buffer layer (triangles) extends the accessible T_{lum}−ΔT_{sol} parameter space further compared to the single use of an AR layer (diamonds). The spread in ΔT_{sol} (T_{lum}) for these multilayer structures reflects the margin of error obtained when reproducing these multilayers. These occur due to slight differences in growth parameters like base pressure, target poisoning, or initial surface temperature of the substrate. These differences cause small variations in thickness, roughness, and density of the individual layers and somewhat affect the overall optical performance of the multilayer architecture. However, all the above statements concerning superior performance using AR layers are valid only when an anatase AR layer is utilized. The performance significantly diminishes when a rutile AR layer is used, cf. green pentagons in Figure 4, independent of its thickness. This phenomenon has been previously discussed and is attributed to the oxidation of VO_2 to V_2O_5 during the sputtering process.

By forming a thermochromic trilayer coating with 50 nm VO_2 as an active layer, a R-TiO_2 buffer, and an A-TiO_2 AR layer, we were able to enhance the key optical parameters, T_{lum} and ΔT_{sol}, by 5−8% each. However, it is important to note that T_{lum}, in particular, still requires further enhancement, which may be accomplished through the additional doping of the functional VO_2 film. Regarding the discrepancies observed between simulation and experimental results, it is noteworthy that the simulations discussed thus far have only assumed ideal interfaces between the various layers of the architecture as discussed above. In reality, however, a deposited film will exhibit a certain surface roughness leading to interface roughness in the multilayer structures; thus, they may not be considered ideal. This interface roughness will also affect the optical properties of multilayer structures. These factors can be addressed in the simulations making use of the effective medium (EM) approximation. Additional interface layers may be included in the simulation, and the EM approximation can be employed to calculate the refractive index of a composite that represents the mixture of two phases at the interface.

https://doi.org/10.1021/acsaelm.5c01043
ACS Appl. Electron. Mater. 2025, 7, 7668−7678

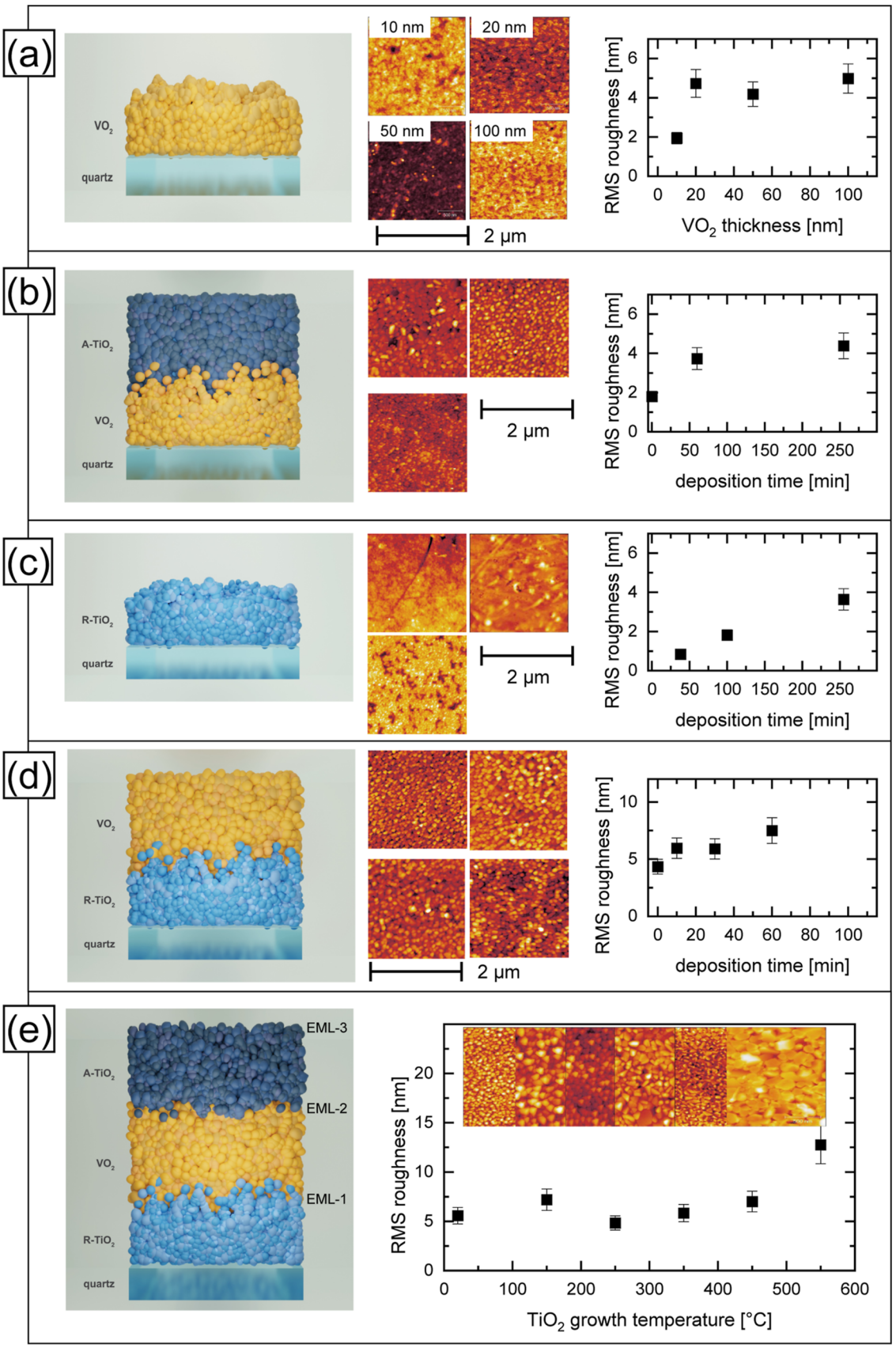

Figure 5. (a) Schematic of an architecture VO_2||glass (left), AFM images of the corresponding surfaces of samples with different thicknesses (center), and the RMS roughness determined from those images (right). (b–e) Corresponding data sets of architectures A-TiO_2/VO_2||glass (b), R-TiO_2||glass (c), VO_2/R-TiO_2||glass (d), and A-TiO_2/VO_2/R-TiO_2||glass (e).

https://doi.org/10.1021/acsaelm.5c01043
ACS Appl. Electron. Mater. 2025, 7, 7668−7678

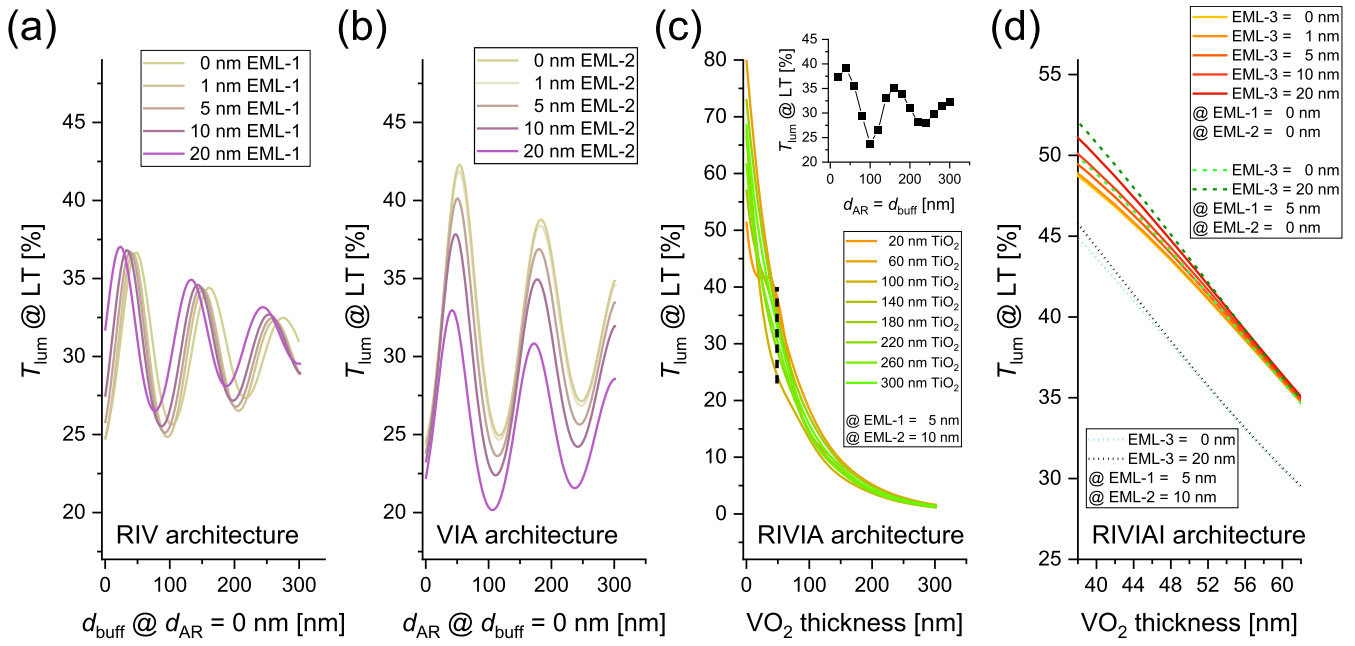

Figure 6. T_{lum} as a function of the thickness of the TiO_2 buffer layer (a) and the TiO_2 AR layer (b). The lines represent data calculated using different thicknesses of the interface layers EML-1 and EML-2, respectively. (c) T_{lum} as a function of the thickness of the VO_2 layer for architectures with additional interface layers EML-1 (5 nm) and EML-2 (10 nm). The dashed line represents the values taken for the inset. This inset shows the dependence of T_{lum} at a distinct VO_2 thickness of 50 nm on the thickness of the layers TiO_2-1 and TiO_2-2, chosen to be the same. (d) T_{lum} as a function of the thickness of the VO_2 layer for architectures with additional interface layers EML-3 (solid lines). We further assess the combined impact of EML-3 with EML-1 (dashed lines) as well as EML-1 and EML-2 (dotted lines).

Specifically, we utilize Bruggeman's model to determine the optical constants of the interface layer. For modeling the surface and interfaces, we include additional interface layers—effective-medium layers (EML)—in the multilayer model. These interface layers are designated as EML-x, where x runs from 1 to 3. In detail, EML-1 denotes the interface layer between the rutile TiO_2 buffer layer and the functional VO_2 layer, whereas EML-2 corresponds to the interface layer between the functional VO_2 layer and the anatase TiO_2 top layer. Finally, EML-3 denotes the interface layer between the anatase TiO_2 top layer and air and thus reflects the surface roughness of the multilayer architecture. The thickness of each individual EML is taken from the experimentally measured surface roughness data of the corresponding lower layer (in case of EML-1 and 2 recorded prior to growing the next layer). Figure 5a presents a schematic of the VO_2||glass architecture (left), AFM images showcasing the surfaces of samples with varying thicknesses (center), and a plot of root-mean-square (RMS) roughness versus thickness (right). Figure 5b−e provides comparable data for other architectures, such as A-TiO_2/VO_2||glass (b), R-TiO_2||glass (c), VO_2/R-TiO_2||glass (d), and A-TiO_2/VO_2/R-TiO_2||glass (e). In every case, we observe that RMS roughness increases with layer thickness, eventually reaching a plateau at larger thicknesses. While the input of thermal energy increases with deposition time, the roughness observed is ultimately constrained by the substrate temperature.

The refractive indices of TiO_2 and VO_2, obtained by ellipsometry on our samples, were utilized to assess the optical response of the architectures while considering the effects of surface roughness by incorporating the corresponding EML-x interfaces. Figure 6 presents T_{lum} as a function of the thickness of the R-TiO_2 buffer layer in graph (a) and the thickness of the A-TiO_2 AR layer in graph (b). The curves depicted in these figures correspond to the architectures VO_2/EML-1/R-TiO_2||glass and A-TiO_2/EML-2/VO_2||glass, respectively. Solid lines represent the T_{lum} values computed for varying EML-x thicknesses. In Figure 6a, the interface between the buffer layer and VO_2 has a minimal impact on optical performance, with a slight shift in the modulation curve toward lower buffer thicknesses and a small enhancement in luminous transmittance. Conversely, the presence of an additional interface layer between the AR layer and VO_2 has a pronounced effect on the luminous transmittance, cf. Figure 6b. For example, T_{lum} decreases by 2−3% with a 5 nm interface layer. A reduction by as much as 10 will occur if the interface thickness exceeds 20 nm. AFM measurements reveal that the sputtered architectures exhibit an RMS roughness of up to 10 nm, indicating that the presence of the interface layer may contribute to a reduction of T_{lum} of approximately 4%.

In Figure 6c, the relationship between T_{lum} and the thickness of the VO_2 layer is depicted for various TiO_2 thicknesses within symmetric A-TiO_2/EML-2/VO_2/EML-1/R-TiO_2||glass architectures. Here, the interface layer thicknesses were assumed as EML-1 = 5 nm and EML-2 = 10 nm. A significant decrease in T_{lum} is observed as the VO_2 thickness increases. However, we obtain fluctuations in T_{lum} as a function of the TiO_2 thickness, as emphasized by a dashed line for a 50 nm VO_2 layer. The inset of Figure 6c illustrates that these fluctuations are not random but resemble the curve of a damped oscillation. Consistent with observations from AlN/VO_2/AlN||glass architectures, the correlation between simulation results and experimental data improves when interface considerations are included.[22] Additionally, incorporating a third upper interface layer, EML-3, into symmetric configurations such as EML-3/A-TiO_2/EML-2/VO_2/EML-1/R-TiO_2||glass does not notably alter the optical response, as demonstrated in Figure 6d. The T_{lum} values show only a minor

https://doi.org/10.1021/acsaelm.5c01043
ACS Appl. Electron. Mater. 2025, 7, 7668−7678

variation with an increase in EML-3 thickness (solid lines). Assuming an additional non-negligible interface between the buffer layer and VO_2 (EML-1 = 5 nm) does not change this finding significantly (dashed lines). Conversely, the overall T_{lum} does diminish if we add an additional 10 nm interface layer between the AR layer and VO_2 (EML-2), as illustrated by the dotted lines in Figure 6d. This indicates that EML-1 and, particularly, EML-2 have a more substantial effect on the optical response than does EML-3, which accounts for the surface roughness of the A-TiO_2 AR layer. Hence, EML-3 can be neglected in the modeling of the optical response in the architectures examined in this study. This holds true as well for the key measure, ΔT_{sol}, cf. Figure S5 of the Supporting Information. Again, we find a strong impact of EML-2, whereas EML-1 and especially EML-3 have only a minor impact on the thermochromic performance. Nonetheless, the simulations also underline the expected opposing trends in T_{lum} and ΔT_{sol} and, thus, the need for a careful choice of thicknesses and knowledge of interface roughness.

In summary, the simulated results accounting for interface roughness by effective medium theory align more closely with the experimentally measured T_{lum} values than those obtained from simulations based on ideal interfaces. Let us narrow this statement in more detail. The simulation of ideal multilayer structures without accounting for surface roughness or extended interface layers gave a luminous transmittance of around 45% for an optimized thickness of buffer as well as AR layer, cf. Figure 1a. However, taking into account the actual surface roughness of each constituent layer, we have to include interface layers EML-1 of around 4−5 nm and EML-2 of around 8−10 nm. Doing that, the effective T_{lum} values will decrease to 35−37%, cf. Figure 6, which is in good agreement with the experimental values found, cf. Figure 4. This highlights that realistic modeling of interface roughness is essential for accurate prediction of key quantities in VO_2-based thermochromic architectures.

CONCLUSIONS

This article highlights the potential of integrating TiO_2-based structures to enhance the efficiency of VO_2-based smart windows. Rutile TiO_2 buffer layers are used to promote the growth of VO_2 films. Additionally, TiO_2 antireflection coatings can improve the optical performance of smart windows by minimizing reflections and maximizing light transmission. The proposed multilayer architecture holds promise for advancing the development of energy-efficient building technologies.

ASSOCIATED CONTENT

Supporting Information

The Supporting Information is available free of charge at https://pubs.acs.org/doi/10.1021/acsaelm.5c01043.

X-ray diffractograms and Raman spectra of TiO_2 and VO_2 layers, demonstrating the constituent phases of the multilayer stacks discussed in this work; temperature-dependent ellipsometry to determine the optical constants of TiO_2 and VO_2 in both transition states; scheme of the multilayer architecture R-TiO_2/VO_2/R-TiO_2/glass and contour maps of the thermochromic key quantities T_{lum} (25 °C), T_{lum} (90 °C), and ΔT_{sol} as a function of thickness of the R-TiO_2 buffer layer (x-axis) and that of the R-TiO_2 AR layer (y-axis) with a fixed thickness of VO_2 of 50 nm; simulations of T_{lum} at 25 °C and ΔT_{sol} for multilayer architectures R-TiO_2/V_2O_5/VO_2/R-TiO_2/glass as a function of thickness of the buffer layer (R-TiO_2) and AR layer (R-TiO_2), respectively, for a fixed VO_x thickness of 50 nm; and simulations of ΔT_{sol} as a function of the thickness of the constituent layers accounting for additional interface layers (PDF)

AUTHOR INFORMATION

Corresponding Author

Martin Becker − *Institute for Experimental Physics I and Center for Materials Research (ZfM/LaMa), Justus Liebig University Giessen, Giessen 35392, Germany;* orcid.org/0000-0002-1199-7892; Email: martin.becker@exp1.physik.uni-giessen.de

Authors

Yan Ravil Wollenweber-Bienerth − *Institute for Experimental Physics I and Center for Materials Research (ZfM/LaMa), Justus Liebig University Giessen, Giessen 35392, Germany*

Saskia Hartmann − *Institute for Experimental Physics I and Center for Materials Research (ZfM/LaMa), Justus Liebig University Giessen, Giessen 35392, Germany*

Angelika Polity − *Institute for Experimental Physics I and Center for Materials Research (ZfM/LaMa), Justus Liebig University Giessen, Giessen 35392, Germany*

Sangam Chatterjee − *Institute for Experimental Physics I and Center for Materials Research (ZfM/LaMa), Justus Liebig University Giessen, Giessen 35392, Germany*

Peter J. Klar − *Institute for Experimental Physics I and Center for Materials Research (ZfM/LaMa), Justus Liebig University Giessen, Giessen 35392, Germany;* orcid.org/0000-0002-4513-0330

Complete contact information is available at: https://pubs.acs.org/10.1021/acsaelm.5c01043

Author Contributions

M.B. conceived the topic discussed in this paper; M.B. synthesized the thin films; M.B., Y.R.W., and S.H. performed the experiments; M.B. performed the simulations; M.B., S.C., and P.J.K. acquired the funding; M.B. and P.J.K. primarily wrote the main manuscript text. All authors have given approval to the final version of the manuscript.

Funding

Financial support was provided by the BMBF (Bundesministerium für Bildung and Forschung) within the IntelVanaGlas (03VP09691) project. M.B. acknowledges financial support by the DFG under research grant 510965362.

Notes

The authors declare no competing financial interest.

ACKNOWLEDGMENTS

The authors thank Elisa Monte for graphical work and Jonas Hauptmann for valuable impact concerning the simulations.

REFERENCES

(1) Li, S.-Y.; Niklasson, G. A.; Granqvist, C. G. Thermochromic fenestration with VO_2-based materials: Three challenges and how they can be met. *Thin Solid Films* **2012**, *520*, 3823−3828.

(2) Hoffmann, S.; Lee, E. S.; Clavero, C. Examination of the technical potential of near-infrared switching thermochromic windows

https://doi.org/10.1021/acsaelm.5c01043
ACS Appl. Electron. Mater. 2025, 7, 7668−7678

for commercial building applications. *Sol. Energy Mater. Sol. Cells* **2014**, *123*, 65−80.
(3) Rashidzadeh, Z.; Heidari Matin, N. A Comparative Study on Smart Windows Focusing on Climate-Based Energy Performance and Users' Comfort Attributes. *Sustainability* **2023**, *15*, 2294.
(4) Jiang, C.; He, L.; Xuan, Q.; Liao, Y.; Dai, J.-G.; Lei, D. Phase-change: VO_2-based thermochromic smart windows. *Light: Sci. Appl.* **2024**, *13*, 255.
(5) Goodenough, J. B. The two components of the crystallographic transition in VO_2. *J. Solid State Chem.* **1971**, *3*, 490−500.
(6) Ke, Y.; Wang, S.; Liu, G.; Li, M.; White, T. J.; Long, Y. Vanadium Dioxide: The Multistimuli Responsive Material and Its Applications. *Small* **2018**, *14*, 1802025.
(7) Tselev, A.; Luk'yanchuk, I. A.; Ivanov, I. N.; Budai, J. D.; Tischler, J. Z.; Strelcov, E.; Kolmakov, A.; Kalinin, S. V. Symmetry Relationship and Strain-Induced Transitions between Insulating M1 and M2 and Metallic R phases of Vanadium Dioxide. *Nano Lett.* **2010**, *10*, 4409−4416.
(8) Strelcov, E.; Tselev, A.; Ivanov, I.; Budai, J. D.; Zhang, J.; Tischler, J. Z.; Kravchenko, I.; Kalinin, S. V.; Kolmakov, A. Doping-Based Stabilization of the M2 Phase in Free-Standing VO_2 Nanostructures at Room Temperature. *Nano Lett.* **2012**, *12*, 6198−6205.
(9) Ji, Y.; Zhang, Y.; Gao, M.; Yuan, Z.; Xia, Y.; Jin, C.; Tao, B.; Chen, C.; Jia, Q.; Lin, Y. Role of microstructures on the M1-M2 phase transition in epitaxial VO_2 thin films. *Sci. Rep.* **2014**, *4*, 4854.
(10) Burkhardt, W.; Christmann, T.; Franke, S.; Kriegseis, W.; Meister, D.; Meyer, B. K.; Niessner, W.; Schalch, D.; Scharmann, A. Tungsten and fluorine co-doping of VO_2 films. *Thin Solid Films* **2002**, *402*, 226−231.
(11) Dietrich, M.; Kuhl, F.; Polity, A.; Klar, P. J. Optimizing thermochromic VO_2 by co-doping with W and Sr for smart window applications. *Appl. Phys. Lett.* **2017**, *110*, 141907.
(12) Shen, N.; Chen, S.; Shi, R.; Niu, S.; Amini, A.; Cheng, C. Phase Transition Hysteresis of Tungsten Doped VO_2 Synergistically Boosts the Function of Smart Windows in Ambient Conditions. *ACS Appl. Electron. Mater.* **2021**, *3*, 3648−3656.
(13) Chen, L.; Hu, H.; Cui, Y.; Gao, Y. Hydrogenatio-triggered phase transition in W-doped VO_2: A first-principles calculations. *Mater. Today Commun.* **2025**, *43*, 111683.
(14) Suzuki, H.; Yamaguchi, K.; Miyazaki, H. Fabrication of thermochromic composite using monodispersed VO_2 coated SiO_2 nanoparticles prepared by modified chemical solution deposition. *Compos. Sci. Technol.* **2007**, *67*, 3487−3490.
(15) Hao, Q.; Li, W.; Xu, H.; Wang, J.; Yin, Y.; Wang, H.; Ma, L.; Ma, F.; Jiang, X.; Schmidt, O. G.; Chu, P. K. VO_2/TiN Plasmonic Thermochromic Smart Coatings for Room-Temperature Applications. *Adv. Mater.* **2018**, *30*, 1705421.
(16) Zhao, X.; Hu, X.; Sun, J.; You, Q.; Xu, H.; Liu, W.; Sun, G.; Nie, Y.; Yao, W.; Jiang, X. VO_2-based composite films with exemplary thermochromic and photochromic performance. *J. Appl. Phys.* **2020**, *128*, 185107.
(17) Dietrich, M.; Kramm, B. G.; Becker, M.; Meyer, B. K.; Polity, A.; Klar, P. J. Influence of doping with alkaline earth metals on the optical properties of thermochromic VO_2. *J. Appl. Phys.* **2015**, *117*, 185301.
(18) Kuhl, F.; Becker, M.; Benz, S. L.; Hauptmann, J.; Kessler, J.; Chatterjee, S.; Polity, A.; Klar, P. J. Embedding Quaternary $V_{1-x-y}Sr_xW_yO_2$ into Multilayer Systems to Enhance Its Thermochromic Properties for Smart Glass Applications. *ACS Appl. Electron. Mater.* **2022**, *4*, 513−520.
(19) Kaufman, M.; Vlček, J.; Houška, J.; Farrukh, S.; Haviar, S.; Čerstvý, R.; Kozak, T. A low-temperature synthesis of strongly thermochromic W and Sr co-doped VO_2 films with a low transition temperature. *J. Appl. Phys.* **2024**, *136*, 215301.
(20) Long, S.; Zhou, H.; Bao, S.; Xin, Y.; Cao, X.; Jin, P. Thermochromic multilayer films of WO_3/VO_2/WO_3 sandwich structure with enhanced luminous transmittance and durability. *RSC Adv.* **2016**, *6*, 106435.
(21) Jin, W.; Park, K.; Cho, J. Y.; Bae, S.-H.; Siyar, M.; Jang, H.; Park, C. Thermochromic properties of ZnO/VO_2/ZnO films on soda lime silicate glass deposited by RF magnetron sputtering. *Ceram. Int.* **2023**, *49*, 10437−10444.
(22) Becker, M.; Wollenweber-Bienerth, Y. R.; Hauptmann, J.; Celik, E.; Polity, A.; Chatterjee, S.; Klar, P. J. Assessing AlN||VO_2||AlN Multilayer Architectures Deposited by Ion Beam Sputtering for Smart Window Applications. *ACS Appl. Electron. Mater.* **2024**, *6* (8), 6049−6058.
(23) Suresh, E. K.; Arun, B.; Andrews, J.; Akhil Raman, T. S.; Nikhil Mohan, P.; Shivakumar, C.; James Raju, K. C. Role of buffer layers on the strain-induced insulator-metal transition of VO_2 thin films: a review. *Crit. Rev. Solid State Mater. Sci.* **2024**, *50*, 137−160.
(24) Kang, L.; Gao, Y.; Luo, H.; Chen, Z.; Du, J.; Zhang, Z. Nanoporous Thermochromic VO_2 Films with Low Optical Constants, Enhanced Luminous Transmittance and Thermochromic Properties. *ACS Appl. Mater. Interfaces* **2011**, *3*, 135−138.
(25) Cao, X.; Wang, N.; Law, J. Y.; Loo, S. C. J.; Magdassi, S.; Long, Y. Nanoporous Thermochromic VO_2 (M) Thin Films: Controlled Porosity, Largely Enhanced Luminous Transmittance and Solar Modulating Ability. *Langmuir* **2014**, *30*, 1710−1715.
(26) Wang, S.; Xu, H.; Zhang, X.; Yang, S.; Jiang, X. 2D ordered porous VO_2-based composite film with enhanced thermochromism performance and high stability for smart windows. *Ceram. Int.* **2024**, *50*, 35265−35272.
(27) Koo, H.; Xu, L.; Ko, K.-E.; Ahn, S.; Chang, S.-H.; Park, C. Effect of Oxide Buffer Layer on the Thermochromic Properties of VO_2 Thin Films. *JMEPEG* **2013**, *22*, 3967−3973.
(28) Kim, H.; Bingham, N. S.; Charipar, N. A.; Piqué, A. Strain effect in epitaxial VO_2 thin films grown on sapphire substrates using SnO_2 buffer layers. *AIP Adv.* **2017**, *7*, 105116.
(29) Zhang, Z.; Gao, Y.; Kang, L.; Du, J.; Luo, H. Effects of a TiO_2 Buffer Layer on Solution-Deposited VO_2 Films: Enhanced Oxidization Durability. *J. Phys. Chem. C* **2010**, *114*, 22214−22220.
(30) Muraoka, Y.; Hiroi, Z. Metal−insulator transition of VO_2 thin films grown on TiO_2 (001) and (110) substrates. *Appl. Phys. Lett.* **2002**, *80*, 583−585.
(31) Fan, L. L.; Chen, S.; Luo, Z. L.; Liu, Q. H.; Wu, Y. F.; Song, L.; Ji, D. X.; Wang, P.; Chu, W. S.; Gao, C.; Zou, C. W.; Wu, Z. Y. Strain Dynamics of Ultrathin VO_2 Film Grown on TiO_2 (001) and the Associated Phase Transition Modulation. *Nano Lett.* **2014**, *14*, 4036−4043.
(32) Lu, H.; Li, L.; Tang, Z.; Xu, M.; Zheng, Y.; Becker, M.; Lu, Y.; Li, M.; Li, P.; Zhang, Z.; Klar, P. J.; He, Y. Correlation of metal-to-insulator transition and strain state of VO_2 thin films on TiO_2 (110) substrates. *Appl. Phys. Lett.* **2023**, *123*, 042103.
(33) Becker, M.; Kuhl, F.; Hauptmann, J.; Kessler, J.; Benz, S. L.; Chatterjee, S.; Polity, A.; Klar, P. J. Employing Ion-Beam Sputter Deposited TiO_2 Buffer Layers for VO_2-Related Devices. *ACS Appl. Electron. Mater.* **2023**, *5*, 3560−3570.
(34) Gao, W.; Wang, C. M.; Wang, H. Q.; Henrich, V. E.; Altman, E. I. Growth and surface structure of vanadium oxide on anatase (001). *Surf. Sci.* **2004**, *559*, 201−213.
(35) Ji, Y.; Mattsson, A.; Niklasson, G. A.; Granqvist, C. G.; Österlund, L. Synergistic TiO_2/VO_2 Window Coating with Thermochromism, Enhanced Luminous Transmittance, and Photocatalytic Activity. *Joule* **2019**, *3*, 2457−2471.
(36) Zheng, J.; Bao, S.; Jin, P. TiO_2(R)/VO_2(M)/TiO_2(A) multilayer film as smart window: Combination of energy-saving, antifogging and self-cleaning functions. *Nano Energy* **2015**, *11*, 136−145.
(37) Leroy, S.; Douali, R.; Legrand, C.; Krasinski, F.; Blanchard, F.; Roussel, P.; Saitzek, S.; Blach, J. F. Influence of Interface on the Charge Carrier Mobility of $La_2Ti_2O_7$ Layered Perovskite Thin Films Measured by the Time-of-Flight Method. *ACS Appl. Electron. Mater.* **2021**, *3*, 3167−3176.
(38) Zia, W.; Malekshahi Byranvand, M.; Rudolph, T.; Rai, M.; Kot, M.; Das, C.; Kedia, M.; Zohdi, M.; Zuo, W.; Yeddu, V.; et al.

https://doi.org/10.1021/acsaelm.5c01043
ACS Appl. Electron. Mater. 2025, 7, 7668−7678

$MAPbCl_3$ Light Absorber for Highest Voltage Perovskite Solar Cells. *ACS Energy Lett.* **2024**, *9*, 1017−1024.
(39) Zhang, Y.; Lin, Y.; Duan, T.; Song, L. Interfacial engineering of heterogenous catalysts for electrocatalysis. *Mater. Today* **2021**, *48*, 115−134.
(40) Becker, M.; Kessler, J.; Kuhl, F.; Benz, S. L.; Chen, L.; Polity, A.; Klar, P. J.; Chatterjee, S. Phase Control of Multivalent Vanadium Oxides VO_x by Ion-Beam Sputter-Deposition. *Phys. Status Solidi A* **2022**, *219*, 2100828.
(41) Becker, M.; Gies, M.; Polity, A.; Chatterjee, S.; Klar, P. J. Materials processing using radio-frequency ion-sources: Ion-beam sputter-deposition and surface treatment. *Rev. Sci. Instrum.* **2019**, *90*, 023901.
(42) Ohsaka, T.; Izumi, F.; Fujiki, Y. Raman Spectrum of Anatase TiO_2. *J. Raman Spectrosc.* **1978**, *7*, 321−324.
(43) Porto, S. P. S.; Fleury, P. A.; Damen, T. C. Raman Spectra of TiO_2, MgF_2, ZnF_2, FeF_2, and MnF_2. *Phys. Rev.* **1967**, *154*, 522−526.
(44) Shibuya, K.; Sawa, A. Polarized Raman scattering of epitaxial vanadium dioxide films with low-temperature monoclinic phase. *J. Appl. Phys.* **2017**, *122*, 015307.
(45) Verleur, H. W.; Barker, A. S., Jr.; Berglund, C. N. Optical Properties of VO_2 between 0.25 and 5 eV. *Phys. Rev.* **1968**, *172*, 788.
(46) Voloshenko, I.; Kuhl, F.; Gompf, B.; Polity, A.; Schnoering, G.; Berrier, A.; Dressel, M. Microscopic nature of the asymmetric hysteresis in the insulator-metal transition of VO_2 revealed by spectroscopic ellipsometry. *Appl. Phys. Lett.* **2018**, *113*, 201906.
(47) Voloshenko, I.; Gompf, B.; Berrier, A.; Schnoering, G.; Kuhl, F.; Polity, A.; Dressel, M. Interplay between electronic and structural transitions in VO_2 revealed by ellipsometry. *J. Vac. Sci. Technol. B* **2019**, *37*, 061202.
(48) Houška, J.; Kolenaty, D.; Vlček, J.; Barta, T.; Rezek, J.; Čerstvý, R. Significant improvement of the performance of $ZrO_2/V_{1-x}W_xO_2/ZrO_2$ thermochromic coatings by utilizing a second-order interference. *Sol. Energy Mater. Sol. Cells* **2019**, *191*, 365−371.

https://doi.org/10.1021/acsaelm.5c01043
ACS Appl. Electron. Mater. 2025, 7, 7668−7678